*Publ. Astron. Soc. Japan* (2016) 68 (1), 16 (1–16)
doi: 10.1093/pasj/psv124
Advance Access Publication Date: 2016 January 12

# Radiation hydrodynamic simulations of line-driven disk winds for ultra-fast outflows

**Mariko Nomura,[1,*] Ken Ohsuga,[2,3] Hiroyuki R. Takahashi,[2] Keiichi Wada,[4] and Tessei Yoshida[2]**

[1]University of Tsukuba, Center for Computational Sciences, 1-1-1 Tennodai, Tsukuba, Ibaraki 305-8577, Japan
[2]National Astronomical Observatory of Japan, 2-21-1 Osawa, Mitaka, Tokyo 181-8588, Japan
[3]School of Physical Sciences, Graduate University of Advanced Study (SOKENDAI), Shonan Village, Hayama, Kanagawa 240-0193, Japan
[4]Graduate School of Science and Engineering, Kagoshima University, 1-21-35 Korimoto, Kagoshima, Kagoshima 890-0065, Japan

*E-mail: nomura@ccs.tsukuba.ac.jp

Received 2014 October 27; Accepted 2015 November 26

## Abstract

Using two-dimensional radiation hydrodynamic simulations, we investigate the origin of the ultra-fast outflows (UFOs) that are often observed in luminous active galactic nuclei (AGNs). We found that the radiation force due to the spectral lines generates strong winds (line-driven disk winds) that are launched from the inner region of accretion disks ($\sim$30 Schwarzschild radii). A wide range of black hole masses ($M_{\rm BH}$) and Eddington ratios ($\varepsilon$) was investigated to study the conditions causing the line-driven winds. For $M_{\rm BH} = 10^6$–$10^9\,M_\odot$ and $\varepsilon = 0.1$–$0.7$, funnel-shaped disk winds appear, in which dense matter is accelerated outward with an opening angle of 70°–80° and with 10% of the speed of light. If we observe the wind along its direction, the velocity, the column density, and the ionization state are consistent with those of the observed UFOs. As long as obscuration by the torus does not affect the observation of X-ray bands, the UFOs could be statistically observed in about 13%–28% of the luminous AGNs, which is not inconsistent with the observed ratio ($\sim$40%). We also found that the results are insensitive to the X-ray luminosity and the density of the disk surface. Thus, we can conclude that UFOs could exist in any luminous AGNs, such as narrow-line Seyfert 1s and quasars with $\varepsilon > 0.1$, with which fast line-driven winds are associated.

**Key words:** accretion — accretion disks—galaxies: active—methods: numerical

## 1 Introduction

Outflows are frequently observed in active galactic nuclei (AGNs) and their origin has been discussed. Blueshifted absorption lines in the spectra suggest the existence of the outflows. Typical absorption lines are broad absorption lines (BALs), of which the blueshifted velocities are $\sim$10000 km s$^{-1}$ and the line widths exceed 2000 km s$^{-1}$ (Weymann et al. 1991; Hamann et al. 1993; Gibson et al. 2009; Allen et al. 2011). BALs are observed in optical or ultraviolet (UV) spectra and detected in 10%–20% of quasars. The blueshifted absorption lines are also observed in the X-ray band (e.g., Pounds et al. 2003;

Tombesi et al. 2010). Such absorption features are thought to be made by Fe XXV and/or Fe XXVI in the outflow. The velocity and the column density of the outflow are roughly evaluated as 0.1–0.3$c$ and $10^{22}$–$10^{24}$ cm$^{-2}$, where $c$ is the speed of light. These high-velocity outflows are called ultra-fast outflows (UFOs). Though the number of samples is still small, UFOs are detected in about half of Seyfert galaxies. Since the kinetic luminosity of the UFOs is evaluated to be comparable to or larger than that of jets (Tombesi et al. 2012a), the UFOs may contribute to the AGN feedback. In addition, the mass outflow rate of UFOs is at least 5%–10% of the mass accretion rate onto the black holes. Thus, UFOs may have an impact on the growth of supermassive black holes. However, the origin of UFOs is still unknown.

The dichotomy between the AGNs with the absorption lines and those without is a problem still in discussion. Weymann et al. (1991) suggested that the difference between them is caused by the viewing angle of the observer, since the properties other than the absorption lines are quite similar between BAL and non-BAL quasars. Elvis (2000) proposed the funnel-shaped disk wind model. In this model, if the wind interrupts the observer's line of sight (the observer's viewing angle coincides with the opening angle of the wind), the blueshifted absorption lines appear in the spectra. In contrast, if there is no wind between the nuclei and the observer, the absorption features are not detected. On the other hand, Zubovas and King (2013) have proposed another idea: that the outflows appear intermittently. In this case, the presence or absence of the absorption features changes with time independently of the viewing angle.

Until now, many theoretical models have been proposed to explain the origin of the outflow. One of the most plausible models is line-driven disk winds, in which radiation force due to spectral lines (the absorbing of UV radiation through the bound–bound transition of metals) accelerates the matter and launches the outflows from the disk surface. This mechanism is effective only for matter in a low or moderate ionization state, since the bound–bound transition cannot occur if the metals are fully ionized. Thus, the line-driven wind model is capable of explaining the acceleration and the ionization state of the wind, which are required to reproduce the blueshifted absorption lines, at the same time. The discovery of line locking in some quasars (Foltz et al. 1987) indicates that the line force can play an important role in the acceleration of the matter. Stevens and Kallman (1990) (hereafter SK90) showed that the line-driven mechanism becomes more effective for matter in the low ionization state and the radiation force including the line force can be 10–1000 times larger than the radiation force due to electron scattering. This implies that the line-driven wind can be launched from sub-Eddington disks. The magnetically driven winds can also explain the acceleration of the outflows (Blandford & Payne 1982; Konigl & Kartje 1994; Everett & Murray 2007). However, the extra mechanism is required to realize the optimum ionization state of the metals.

Radiation hydrodynamic simulations of line-driven winds launched from the disks around supermassive black holes have been performed by Proga, Stone, and Kallman (2000) and Proga and Kallman (2004)—hereafter PSK00 and PK04. They improved the numerical method for line-driven winds around white dwarfs (Proga et al. 1998, 1999), and applied to the outflows in AGNs. PSK00 and PK04 reproduced the funnel-shaped disk wind. The wind comes from a distance from the black hole of several $100\,R_{\rm S}$ and goes away in the direction of $\theta \sim 70^\circ$ for the typical parameters, $M_{\rm BH} = 10^8\,M_\odot$ and $\varepsilon = 0.5$, where $R_{\rm S}$ is the Schwarzschild radius, $\theta$ is the polar angle measured from the rotation axis of the disk, $M_{\rm BH}$ is the black hole mass, and $\varepsilon$ is the Eddington ratio of the UV radiation. Based on the results of PK04, Schurch, Done, and Proga (2009) and Sim et al. (2010) performed a spectral synthesis and compared them to the X-ray observations.

Although PSK00 and PK04 mentioned that the winds are produced for the range of $M_{\rm BH} > 10^7\,M_\odot$ and the winds do not appear for $\varepsilon = 0.1$, their simulations focus on the case of $M_{\rm BH} = 10^8\,M_\odot$ and $\varepsilon = 0.5$. Line-driven disk winds in a wide parameter space of black hole mass and Eddington ratio were investigated by Risaliti and Elvis (2010). They used a non-hydrodynamic method, in which the trajectories of the fluid elements are calculated by solving the equation of motion including the line force, and found a steady structure for line-driven winds. Using a similar non-hydrodynamic method, Nomura et al. (2013) also investigated wind properties such as ionization state, outflow velocity, and column density, and compared them to those inferred from X-ray observations of BALs. As a result, it has been concluded that BALs are detected in 10% of AGNs in the case of $M_{\rm BH} \sim 10^7$–$10^8\,M_\odot$ and $\varepsilon \sim 0.3$–$0.9$.

Thus, previous studies focused either only on a typical case using hydrodynamic simulations, or on kinematics of the wind in a wide parameter space without considering hydrodynamic effects. However, radiation hydrodynamic simulations in the wide parameter space have not been performed yet. In previous studies, the line-driven wind model has never been applied to UFOs, although UFOs are detected for a wide variety of black hole masses and Eddington ratios (Tombesi et al. 2011). Since the UFOs are important with respect to the evolution of supermassive black holes and the feedback to the host galaxies, we here

try to understand the origin of the UFOs in the context of the line-driven wind model. In this paper, we investigate the line-driven winds for various black hole masses and UV luminosities by performing two-dimensional radiation hydrodynamic simulations. We also investigate cases when X-ray photoionization is more effective and the density at the disk surface is relatively large or small. In addition, we calculate the ionization parameter, the outflow velocity, and the column density along the line of sight. Then, by comparing them with the observational features of UFOs, we examine whether or not the line-driven wind may explain the phenomena. We explain our calculation method in section 2. We present the results of the simulations and a comparison with the observational features in section 3. We devote sections 4 and 5 to discussion and conclusions.

## 2 Method

### 2.1 Basic equations and setup

The method of calculation is almost the same as that of PSK00 and PK04. We use spherical polar coordinates ($r$, $\theta$, $\varphi$), where $r$ is the distance from the origin of the coordinate, $\theta$ is the polar angle, and $\varphi$ is the azimuthal angle. We assume axial symmetry with respect to the rotation axis of the accretion disk. The basic equations of hydrodynamics are the equation of continuity,

$$\frac{\partial \rho}{\partial t} + \nabla \cdot (\rho \boldsymbol{v}) = 0, \tag{1}$$

the equations of motion,

$$\frac{\partial (\rho v_r)}{\partial t} + \nabla \cdot (\rho v_r \boldsymbol{v}) = -\frac{\partial p}{\partial r} + \rho \left( \frac{v_\theta^2}{r} + \frac{v_\varphi^2}{r} + g_r + f_{\mathrm{rad},r} \right), \tag{2}$$

$$\frac{\partial (\rho v_\theta)}{\partial t} + \nabla \cdot (\rho v_\theta \boldsymbol{v}) = -\frac{1}{r}\frac{\partial p}{\partial \theta} + \rho \left( -\frac{v_r v_\theta}{r} + \frac{v_\varphi^2}{r}\cot\theta + g_\theta + f_{\mathrm{rad},\theta} \right), \tag{3}$$

$$\frac{\partial (\rho v_\varphi)}{\partial t} + \nabla \cdot (\rho v_\varphi \boldsymbol{v}) = -\rho \left( \frac{v_\varphi v_r}{r} + \frac{v_\varphi v_\theta}{r}\cot\theta \right), \tag{4}$$

and the energy equation,

$$\frac{\partial}{\partial t}\left[ \rho \left( \frac{1}{2}v^2 + e \right) \right] + \nabla \cdot \left[ \rho \boldsymbol{v} \left( \frac{1}{2}v^2 + e + \frac{p}{\rho} \right) \right] = \rho \boldsymbol{v} \cdot \boldsymbol{g} + \rho \mathcal{L}, \tag{5}$$

where $\rho$ is the mass density, $v = (v_r, v_\theta, v_\varphi)$ is the velocity, $p$ is the gas pressure, $e$ is the internal energy per unit mass, and $\boldsymbol{g} = (g_r, g_\theta)$ is the gravitational acceleration of the black hole. Since the origin of the coordinate ($r = 0$) in the present simulations is slightly distant from the center of the black hole, the $\theta$-component of the gravitational force is not null. We will explain about the computational domain at the end of this subsection. We assume an adiabatic equation of state $p/\rho = (\gamma - 1)e$ with $\gamma = 5/3$.

In the last terms of equations (2) and (3), $\boldsymbol{f}_{\mathrm{rad}} = (f_{\mathrm{rad},r}, f_{\mathrm{rad},\theta})$ is the radiation force per unit mass including the line of force,

$$\boldsymbol{f}_{\mathrm{rad}} = \frac{\sigma_{\mathrm{e}} \boldsymbol{F}_{\mathrm{D}}}{c} + \frac{\sigma_{\mathrm{e}} \boldsymbol{F}_{\mathrm{D}}}{c} M, \tag{6}$$

where $\sigma_{\mathrm{e}}$ is the mass-scattering coefficient for free electrons, $\boldsymbol{F}_{\mathrm{D}}$ is the flux from the accretion disk, and $M$ is the force multiplier (see sub-subsection 2.4.2). The first term is the radiation force due to electron scattering and the second term is the line force. We simply assume that all photons emitted from the hot region of the accretion disk are able to contribute to the line force. We explain the definition of $F_{\mathrm{D}}$ in sub-subsection 2.4.1.

In the second term on the right-hand side of the equation (5), $\mathcal{L}$ is the net cooling rate (see PSK00),

$$\mathcal{L} = n^2 (G_{\mathrm{Compton}} + G_{\mathrm{X}} - L_{\mathrm{b,l}}), \tag{7}$$

where $n$ is the number density, $G_{\mathrm{Compton}}$ is the Compton heating/cooling rate,

$$G_{\mathrm{Compton}} = 8.9 \times 10^{-36} \xi (T_{\mathrm{X}} - 4T), \tag{8}$$

$G_{\mathrm{X}}$ is the rate of X-ray photoionization heating and recombination cooling,

$$G_{\mathrm{X}} = 1.5 \times 10^{-21} \xi^{1/4} T^{-1/2} (1 - T/T_{\mathrm{X}}), \tag{9}$$

and $L_{\mathrm{b,l}}$ is the bremsstrahlung and line cooling,

$$L_{\mathrm{b,l}} = 3.3 \times 10^{-27} T^{1/2} + 1.7 \times 10^{-18} \xi^{-1} T^{-1/2} \times \exp(-1.3 \times 10^5 / T) + 10^{-24}. \tag{10}$$

In the above three equations, $T$ is the temperature obtained by $T = \mu m_{\mathrm{p}} p / k_{\mathrm{B}} \rho$, where $\mu$ (= 0.5) is the mean molecular weight, $m_{\mathrm{p}}$ is the proton mass, and $k_{\mathrm{B}}$ is the Boltzmann constant. The ionization parameter is denoted by $\xi$ defined as

$$\xi = \frac{4\pi F_{\mathrm{X}}}{n}, \tag{11}$$

where $F_X$ is the X-ray flux (see sub-subsection 2.4.1 for a detailed explanation). We assume the temperature of the X-ray radiation to be $T_X = 10^8$ K, following PSK00.

As with PK04, our computational domain occupies the radial range of $r_i = 30\,R_S \leq r \leq r_o = 1500\,R_S$ and the angular range of $0^\circ \leq \theta \leq 90^\circ$. The plane of $\theta = 90^\circ$ does not correspond to the equatorial plane of the accretion disk, but is located at the surface of the accretion disk. Specifically, this plane is placed in parallel with the equatorial plane at a distance of $z_0$. Here, we set $z_0 = 4.0\varepsilon R_S$, which roughly corresponds to the scale height of the standard disk (Shakura & Sunyaev 1973). Throughout the present study, we employ the standard disk model, which is the source of the radiation and supplies the mass to the disk wind. Since $z_0$ is estimated based on the hydrostatic equilibrium in the vertical direction, it is proportional to the Eddington ratio (Kato et al. 2008). We divide this computational domain into 100 grids for the radial range and 160 grids for the angular range. To achieve good spatial resolution at the inner region and near the disk surface, we use fixed zone size ratios, $\Delta r_{j+1}/\Delta r_j = 1.05$ and $\Delta\theta_k/\Delta\theta_{k+1} = 1.066$. The origin of our coordinate is located at $4.0\varepsilon R_S$ above the center of the black hole, so that the $\theta$-component of the gravitational force is not null [see equation (3)]. Here, we note that the resulting wind structure does not change much if we prepare 150 grids for the radial range, in which case the resolution is 4–10 times better than that for 100 grids at $r \sim 30$–$40\,R_S$, which corresponds the launching region of the wind.

## 2.2 Boundary conditions

We set boundary conditions as follows. We apply the axially symmetric boundary at the rotational axis of the accretion disk, $\theta = 0^\circ$ ($\rho$, $p$, and $v_r$ are symmetric, while $v_\theta$ and $v_\varphi$ are antisymmetric). The outflow boundary conditions are employed at the inner and outer radial boundaries, at $r = r_i$ and $r_o$. All quantities are basically symmetric, but matter can freely leave but not enter the computational domain. At the boundary of $\theta = 90^\circ$, we apply a reflecting boundary ($\rho$, $p$, $v_r$, and $v_\varphi$ are symmetric, but $v_\theta$ is antisymmetric).

At the boundary of $\theta = 90^\circ$, the radial velocity and the rotational velocity are fixed to be null and the Keplerian velocity, respectively. Also, the density is kept constant at $\rho = \rho_0$, and the temperature is fixed at the effective temperature of the standard disk surface. The density, $\rho_0$, corresponds to the density at the photosphere of the accretion disk. Basically, we employ $\rho_0 = 10^{-9}\,\mathrm{g\,cm^{-3}}$. We also investigate other cases of $\rho_0 = 10^{-11}$ and $10^{-7}\,\mathrm{g\,cm^{-3}}$ for comparison (see appendix 2). In reality, the density at the disk surface depends on the black hole mass, the Eddington ratio, and the disk radius. However, in this paper, we set $\rho_0$ to be constant with the disk radius as a free parameter.

## 2.3 Initial conditions

We set the initial conditions based on Proga, Stone, and Drew (1998) and PSK00. We assume hydrostatic equilibrium in the vertical direction; then the initial density distribution is

$$\rho(r,\theta) = \rho_0 \exp\left(-\frac{GM_{BH}}{2c_s^2 r\tan^2\theta}\right), \tag{12}$$

where $c_s$ is the sound velocity at the disk surface. The initial temperature at a given point, $(r, \theta)$, is set to be $T(r, \theta) = T_{eff}(r\sin\theta)$, where $T_{eff}$ is the effective temperature of the disk [see equation (13)], i.e., there is no temperature gradient in the vertical direction. We set the initial velocity to be $v_r = v_\theta = 0$. The rotational velocity, $v_\varphi$, is given to meet the equilibrium between gravity and the centrifugal force as $v_\varphi = (GM_{BH}/r)^{1/2}\sin\theta$.

## 2.4 Line force

### 2.4.1 Radiative fluxes emitted from central X-ray source and accretion disk

In our simulations, we consider two radiation sources, a point source located at the center of the coordinate and a hot region of the accretion disk located at the equatorial plane. The radiation from the central point source is assumed to contribute the ionization of metals and is called "X-ray" in this paper. We assume that all photons emitted from the high-temperature region of the disk contribute to the line force and note that the ionization due to the high-energy photons (photons of energy above 13.6 eV) emitted from the disk is not taken into account. To estimate the ionization parameter defined by equation (11), we use the X-ray flux that we calculate here. The luminosities of the X-ray source and the accretion disk are described as $L_X = f_X\varepsilon L_{Edd}$ and $L_D = \varepsilon L_{Edd}$, where $\varepsilon$ is the Eddington ratio of the disk luminosity and $f_X$ is the ratio of the X-ray luminosity to the disk luminosity. Basically, we set $f_X = 0.1$, but we employ $f_X = 1$ in subsection 3.4 in order to investigate the wind when the X-ray photoionization is so effective. The disk radiation comes from the geometrically thin and optically thick disk (standard disk) whose effective temperature distribution is given by

$$T_{eff}(r) = T_{in}\left(\frac{r}{r_{in}}\right)^{-3/4}, \tag{13}$$

where $r_{in}(=3\,R_S)$ is the disk inner radius and $T_{in}$ is the effective temperature at $r = r_{in}$. We set $T_{in}$ to meet the

condition of

$$L_{\rm D} = \varepsilon L_{\rm Edd} = \int_{r_{\rm in}}^{r_{\rm out}} 2\pi r \sigma T_{\rm eff}^4 dr, \tag{14}$$

where $\sigma$ is the Stefan–Boltzmann coefficient, and $r_{\rm out}$ is the outer radius of the inner hot region, where we suppose $T_{\rm eff}(r_{\rm out}) = 3 \times 10^3$ K. In the region $r > r_{\rm out}$, the temperature is too cold to emit photons contributing to the line force effectively. We use the simple method in the same manner as PSK00, which supposes that the radiation from the high-temperature ($>3 \times 10^3$ K) region of the accretion disk contributes to the line force. (In PK04, the radiation between 200 Å and 3200 Å is assumed to contribute to the line force.)

Using the X-ray and disk fluxes in the optically thin media, $F_{\rm X,\,thin}$ and $\boldsymbol{F}_{\rm D,\,thin} = (F^r_{\rm D,thin}, F^\theta_{\rm D,thin})$, which are computed before starting the simulations, we evaluate the radial components of the X-ray and disk fluxes as $F_{\rm X} = F_{\rm X,thin} e^{-\tau_{\rm X}}$ and $F^r_{\rm D} = F^r_{\rm D,thin} e^{-\tau_{\rm D}}$. Here, $\tau_{\rm X}$ and $\tau_{\rm D}$ are the optical depths for the X-ray and the disk radiation calculated at each time step. The dilution of the $\theta$-component of the disk flux is supposed to be negligible, $F^\theta_{\rm D} = F^\theta_{\rm D,thin}$.

The disk flux in the optically thin media is obtained by

$$\boldsymbol{F}_{\rm D,\,thin}(r,\theta) = \int \frac{\sigma T_{\rm eff}^4}{\pi} \boldsymbol{n} d\Omega, \tag{15}$$

where $\boldsymbol{n}$ is the unit vector, and $d\Omega$ is the solid angle from the point $(r, \theta)$ to the infinitesimal surface element of the disk. Here, the disk radiation is supposed to come from the equatorial plane. The X-ray radiation is spherically symmetrical, and the radial component of the X-ray flux in the optically thin media is $F_{\rm X,\,thin} = L_{\rm X}/4\pi r^2$.

We calculate the optical depths for the X-ray and the radiation from the accretion disk as

$$\tau_{\rm X}(r,\theta) = \int_{r_{\rm i}}^{r} \sigma_{\rm X}(\xi)\rho(r',\theta) dr', \tag{16}$$

and

$$\tau_{\rm D}(r,\theta) = \int_{r_{\rm i}}^{r} \sigma_{\rm e}\rho(r',\theta) dr', \tag{17}$$

where $\sigma_{\rm X}$ is the mass extinction coefficient for X-ray. We set $\sigma_{\rm X} = \sigma_{\rm e}$ for $\xi \geq 10^5$ and $\sigma_{\rm X} = 100\sigma_{\rm e}$ for $\xi < 10^5$ in order to include the effects of photoelectronic absorption.

### 2.4.2 Force multiplier

To evaluate the line force, we use the force multiplier proposed by SK90, which is a modified version of that used by Castor, Abbott, and Klein (1975). The force multiplier is the ratio of the line force to the radiation force due to electron scattering and is written as

$$M(t,\xi) = kt^{-0.6}\left[\frac{(1+t\eta_{\rm max})^{0.4} - 1}{(t\eta_{\rm max})^{0.4}}\right]. \tag{18}$$

Here, $t$ is the local optical depth parameter,

$$t = \sigma_{\rm e}\rho v_{\rm th}\left|\frac{dv}{ds}\right|^{-1}, \tag{19}$$

where $v_{\rm th}$ is the thermal speed of the gas, and $dv/ds$ is the velocity gradient along the light-ray. In equation (18), $k$ and $\eta_{\rm max}$ are functions of the ionization parameter, $\xi$, and are written as

$$k = 0.03 + 0.385\exp(-1.4\xi^{0.6}), \tag{20}$$

and

$$\log_{10}\eta_{\rm max} = \begin{cases} 6.9\exp(0.16\xi^{0.4}) & \log\xi \leq 0.5 \\ 9.1\exp(-7.96\times10^{-3}\xi) & \log\xi > 0.5 \end{cases}. \tag{21}$$

The force multiplier formally depends on the thermal speed through the local optical depth parameter, but in other modified models, the line force is given in a form independent of the thermal speed (e.g., Gayley 1995). We set $v_{\rm th} = 20\,{\rm km\,s^{-1}}$ in the same way as PSK00, which corresponds to the thermal speed of hydrogen gas whose temperature is 25000 K. The force multiplier depends on the direction of the light-ray thorough $dv/ds$. However, in our simulations, we approximate the velocity gradient along the light-ray by the velocity gradient in the radial direction,

$$\frac{dv}{ds} \simeq \frac{dv_r}{dr}. \tag{22}$$

By this approximation, the force multiplier becomes independent of the direction and is determined locally. By calculating the ionization parameter, $\xi$, and the local optical depth parameter, $t$, we evaluate the force multiplier at each time step.

## 2.5 Numerical code

The numerical procedure is divided into the following steps. (i) The optical depths for the radiation emitted from the disk and X-ray are calculated by solving equations (16) and (17). Using the optical depths, the radiation fluxes are evaluated (sub-subsection 2.4.1) and we calculate the force multiplier (sub-subsection 2.4.2) as well as the radiation force including the line force [equation (6)]. (ii) Equations (1)–(4), and the energy equation [equation (5)] except for the net cooling term, are calculated. We treat the radiation force as

the external force term explicitly. Here, the hydrodynamic terms for an ideal fluid are solved using an approximate Riemann solver, the HLL method (Harten et al. 1983). The numerical code we use here is taken from Takahashi and Ohsuga (2013). (iii) The temperature (i.e., internal energy of the fluid) is implicitly updated by considering the net cooling rate using the bisection method.

At step (ii), the internal energy sometimes becomes negative for the case where the velocity is very large. In that case, we evaluate the gas pressure (internal energy) from the entropy equation instead of the energy equation,

$$\frac{\partial s}{\partial t} + \nabla \cdot (s\boldsymbol{v}) = (\gamma - 1)\rho^{2-\gamma}\mathcal{L}, \tag{23}$$

where $s$ is the entropy density, $s = p/\rho^{\gamma - 1}$. Finally, we set the lower limits of the density to be $10^{-22}\,\mathrm{g\,cm^{-3}}$ and the temperature to be $T_{\rm eff}(r\sin\theta)$. If the density or the temperature is lower than these, we replace them with the lower limits.

The time step is determined using the Courant–Friedrichs–Levi condition. At each grid, we calculate

$$\Delta t = 0.05\frac{\min(\Delta r, r\,\Delta\theta)}{\sqrt{(v_r + c_{\rm s})^2 + (v_\theta + c_{\rm s})^2}}, \tag{24}$$

where $\Delta r$ and $\Delta\theta$ are the grid sizes in the radial and polar directions. The minimum value of $\Delta t$ in all grids is used as the time step.

## 3 Results

The resulting wind structures for $\varepsilon = 0.5$, $M_{\rm BH} = 10^8\,M_\odot$, $f_{\rm X} = 0.1$, and $\rho_0 = 10^{-9}\,\mathrm{g\,cm^{-3}}$ (hereafter called the "fiducial model") are consistent with the results of PSK00 and PK04. The high-density matter with $2.5 \lesssim \log\xi \lesssim 5.5$ is blown away via the line force, producing a funnel-shaped disk wind with an opening angle of $\sim 78^\circ$ (see figure 1). In appendix 1, we explain the launching mechanism and the dynamics of the wind in detail.

### 3.1 Comparison with observational features of UFOs

Here, we concentrate on the comparison between the results of our simulations and the observations of UFOs. Specifically, we investigate the ionization parameter, the outward velocity, and the column density along the line of sight (from an observer to the origin of the coordinates) based on our results. Then, we calculate the probability of detecting UFOs (UFO probability). The definition of UFOs is that the blueshift of the absorption lines of Fe XXV and/or Fe XXVI is larger than $10000\,\mathrm{km\,s^{-1}}$. Based on Tombesi et al. (2011), the ionization parameter spans $2.5 \lesssim \log\xi \lesssim 5.5$, and the

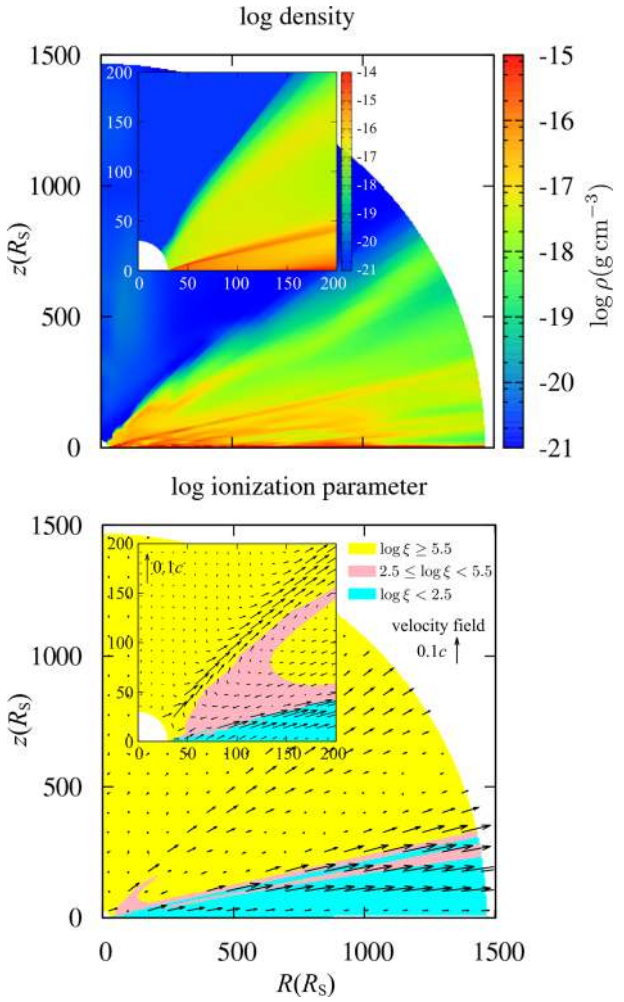


**Fig. 1.** Time averaged density map (top panel) and the ionization parameter map (bottom panel) for $\varepsilon = 0.5$, $M_{\rm BH} = 10^8\,M_\odot$, $f_{\rm X} = 0.1$, and $\rho_0 = 10^{-9}\,\mathrm{g\,cm^{-3}}$. In the bottom panel, the yellow, pink, and cyan show the regions in which the ionization parameters are $\log\xi \geq 5.5$, $2.5 \leq \log\xi < 5.5$, and $\log\xi < 2.5$, respectively. The foreground vectors show the velocity field. The $z = 0$ plane corresponds to the accretion disk surface whose height is $z_0 = 2\,R_{\rm S}$. The $z$-axis is the rotational axis of the accretion disk. (Color online)

column density is distributed in $22 \lesssim \log N_{\rm H} \lesssim 24$. Thus, we recognize the UFO features to be detected if the following conditions (A) and (B) are satisfied: (A) The outward velocity of matter with $2.5 \leq \log\xi < 5.5$ exceeds $10000\,\mathrm{km\,s^{-1}}$. (B) The column density of matter with $2.5 \leq \log\xi < 5.5$ is larger than $10^{22}\,\mathrm{cm^{-2}}$. We evaluate these conditions along the line of sight with viewing angles between $\theta = 0^\circ$ and $90^\circ$, and calculate the solid angle, $\Omega_{\rm UFO}$, within which the UFOs could be observed. We estimate the UFO probability as $\Omega_{\rm UFO}/4\pi$.

Figure 1 shows the time-averaged wind structure of the fiducial model in the $R$–$z$ plane, where the $z$-axis corresponds to the rotation axis of the disk and $R$ is the distance from the rotation axis. The top panel shows the density map. The bottom panel shows the ionization parameter

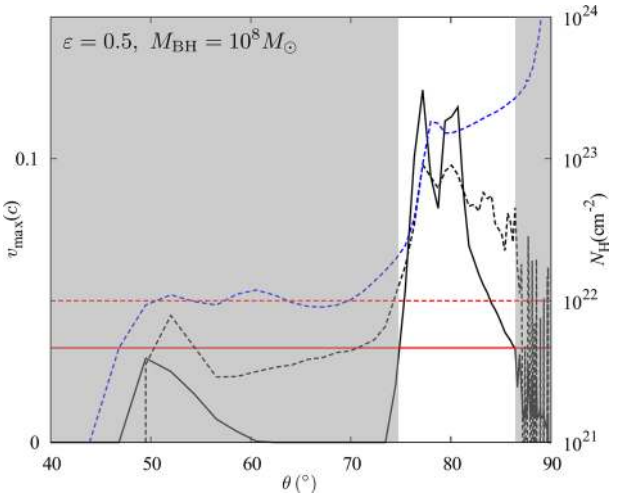


**Fig. 2.** Column density (dashed blue line), column density of the matter with $2.5 \leq \log\xi < 5.5$ (dashed line), and maximum velocity of the matter with $2.5 \leq \log\xi < 5.5$ (solid line) based on the time-averaged results. The abscissa is the viewing angle. The ordinate on the left-hand side shows the value of the solid line. The ordinate on the right-hand side shows the value of the dashed line. The red solid line and the red dashed line show the lines of $v_{\rm max} = 10000\,{\rm km\,s^{-1}}$ and $N_{\rm H} = 10^{22}\,{\rm cm^{-2}}$, respectively. (Color online)

map overlaid with the velocity vectors, where the ionization parameter is presented by dividing it into three levels: yellow ($\log\xi \geq 5.5$), pink ($2.5 \leq \log\xi < 5.5$), and cyan ($\log\xi < 2.5$). An extended view of the inner region ($200\,R_{\rm S} \times 200\,R_{\rm S}$) is shown in both panels. The moderately ionized region ($2.5 \leq \log\xi < 5.5$) roughly corresponds to the mainstream of the wind described by the orange slimline structure (see the extended view of the top panel), which is sandwiched by the low-ionization region ($\log\xi < 2.5$) and the fully ionized region ($\log\xi \geq 5.5$). Along the mainstream, the dense matter moves outward with large velocity, $\sim 0.1c$. Thus, if this mainstream gets across the line of sight, blueshifted absorption features due to moderately ionized ions are expected.

Figure 2 shows the column density (dashed blue line), the column density of the matter with $2.5 \leq \log\xi < 5.5$ (dashed black line), and the maximum velocity of the matter with $2.5 \leq \log\xi < 5.5$ (solid black line) based on the time-averaged results. The abscissa is the viewing angle. The ordinate on the left-hand side shows the value of the solid line. The ordinate on the right-hand side shows the value of the dashed lines. The red solid line and the red dashed line indicate $v_{\rm max} = 10000\,{\rm km\,s^{-1}}$ and $N_{\rm H} = 10^{22}\,{\rm cm^{-2}}$, respectively. Conditions (A) and (B) are satisfied in the unshaded region ($75^\circ \lesssim \theta \lesssim 86^\circ$), where the solid black line is above the red solid line and the dashed black line is above the red dashed line. The resulting UFO probability is 20%.

In the region $\theta \lesssim 50^\circ$, there is no dense and fast wind, so neither of the conditions (A) or (B) is satisfied. In the region $50^\circ \lesssim \theta \lesssim 75^\circ$, the column density is around $10^{22}\,{\rm cm^{-2}}$, but a large portion of the matter is highly ionized ($\log\xi \geq 5.5$). In this region, the density is relatively small and the matter is not shielded from X-ray irradiation. As a consequence, the column density of the matter with $2.5 \leq \log\xi < 5.5$ is smaller than $10^{22}\,{\rm cm^{-2}}$. The outflow velocity of the matter with $2.5 \leq \log\xi < 5.5$ is small due to the weak line force.

Near the the disk surface, $\theta \gtrsim 86^\circ$, the radial velocity is too small to satisfy condition (A), since the radial component of the radiation from the disk is roughly proportional to $\cos\theta$ and is attenuated by the high-density matter around the base of the mainstream. The X-ray radiation is also diluted around the base of the mainstream; a large fraction of the matter is in a low-ionization state, $\log\xi < 2.5$ (see the cyan region in the bottom panel of figure 1). Thus, condition (B) is not satisfied, though the column density is $10^{23}$–$10^{24}\,{\rm cm^{-2}}$. We do not expect to observe UFOs if we observe the accretion disk edge-on. Here, we notice that the X-ray spectrum that Tombesi et al. (2011) assume for estimation of the ionization parameter of UFOs (a power-law with a photon index of 2 in the energy range between 13.6 eV and 13.6 keV) is different from that implicitly assumed in this simulation (see subsection 4.2 for a detailed discussion).

### 3.2 Eddington ratio dependence

Here, we discuss the Eddington ratio dependence of the UFO probability. We calculate the disk wind for a wide range of the Eddington ratio while the black hole mass is kept constant here, $M_{\rm BH} = 10^8\,M_\odot$. We find that the UFO probability is around 20% and is less sensitive to the Eddington ratio in the range of $\varepsilon = 0.1$–$0.7$. The time-averaged UFO probabilities are 17%, 19%, 20%, and 27% for $\varepsilon = 0.1$, 0.3, 0.5, and 0.7, respectively. To understand the reason why the UFO probability has roughly the same value for the different Eddington ratios, we compare the wind structure of $\varepsilon = 0.1$ to that of $\varepsilon = 0.5$.

Figure 3 is the same as figure 1, but for $\varepsilon = 0.1$. In almost the whole region, the density is smaller than that for $\varepsilon = 0.5$ (see the top panel). This is because the radiation force is not large enough to accelerate a large amount of matter. Thus, the region with $\log\xi \geq 5.5$ occupies the most volume (see the bottom panel), since the less dense matter is highly ionized by the X-ray. The relatively high-density matter exists only in the region of $R \lesssim 100\,R_{\rm S}$ and $\theta \gtrsim 70^\circ$ (orange). This region has an ionization parameter of $2.5 \leq \log\xi < 5.5$. The density of this region is too small to be $\log\xi < 2.5$, but this region works to shield the X-ray radiation. Thus, behind this region ($R \gtrsim 100\,R_{\rm S}$), the ionization parameters are $2.5 \leq \log\xi < 5.5$ and $\log\xi < 2.5$.

Figure 4 is the same as figure 2, but for $\varepsilon = 0.1$. We find that the angular range in which condition (A) is satisfied is

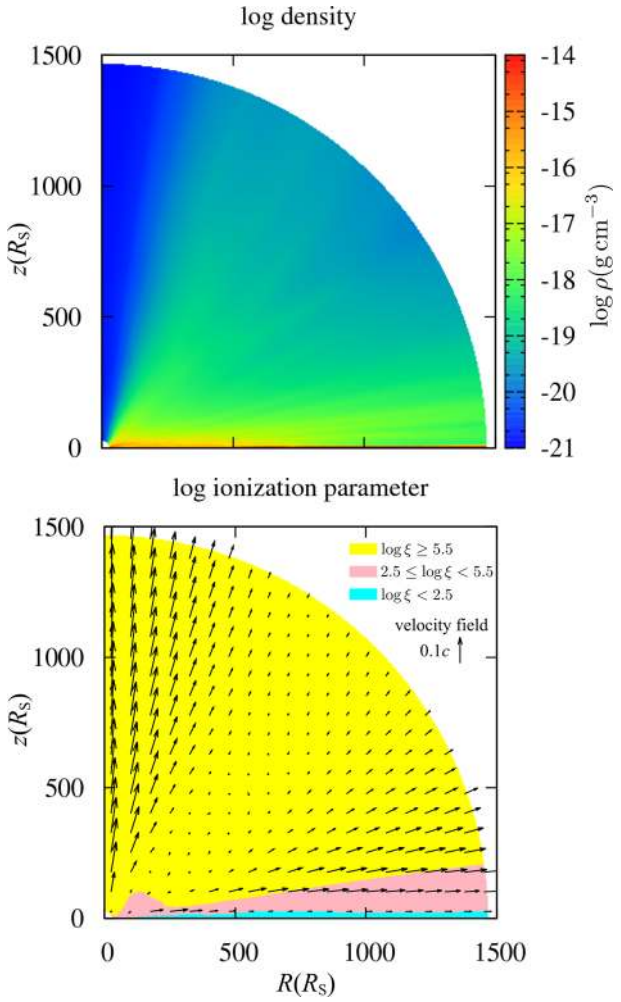


**Fig. 3.** As figure 1, but for $\varepsilon = 0.1$. (Color online)

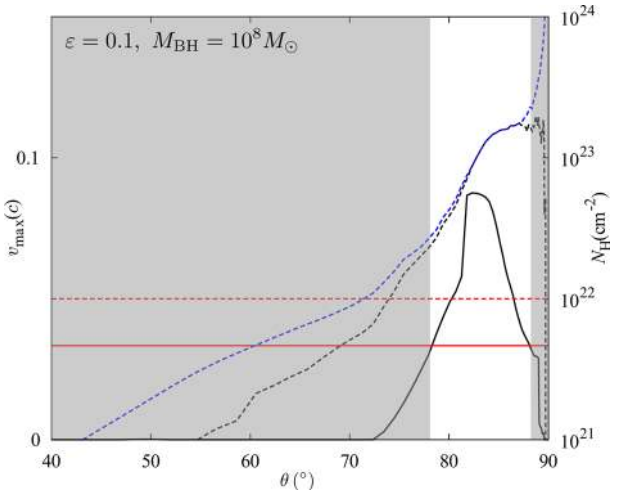


**Fig. 4.** As the top panel of figure 2, but for $\varepsilon = 0.1$. (Color online)

restricted to $\theta \sim 78^\circ$–$88^\circ$, although condition (B) is satisfied at $\theta \gtrsim 73^\circ$. Thus, as compared with that of $\varepsilon = 0.5$, the unshaded region slightly shifts to large $\theta$, but the UFO probability is almost the same. In the unshaded region, we find that the column density is smaller for $\varepsilon = 0.1$ than for $\varepsilon = 0.5$; however, the column density of matter with $2.5 \leq \log\xi < 5.5$ is larger for $\varepsilon = 0.1$ than for $\varepsilon = 0.5$. This is because most of the matter is in a moderate ionization state for $\varepsilon = 0.1$ (see the bottom panel of figure 3). We find that the column density is equal to that of the matter with $2.5 \leq \log\xi < 5.5$. In contrast, for the case with $\varepsilon = 0.5$, a substantial proportion of the matter is in a low ionization state ($\log\xi < 2.5$) in the unshaded region of figure 2. Figure 4 also shows that the maximum velocity slightly decreases with a decline of the Eddington ratio because of the reduced radiation force. For $\varepsilon = 0.1$, the maximum velocity is smaller than $0.1c$.

In the case of $\varepsilon = 0.01$, the disk wind is not launched, since the radiation force is too small to accelerate it. Thus, the UFO probability is zero.

### 3.3 Black hole mass dependence

Next we examine how the UFO probability depends on the black hole mass in a range between $M_{\rm BH} = 10^6\,M_\odot$ and $10^9\,M_\odot$, for a fixed Eddington ratio, $\varepsilon = 0.5$. We find that the funnel-shaped disk winds appear for all cases, and the UFO probability is almost constant or slightly decreases with increasing black hole mass: 28%, 22%, 20%, and 13% for $M_{\rm BH} = 10^6\,M_\odot$, $10^7\,M_\odot$, $10^8\,M_\odot$, and $10^9\,M_\odot$, respectively.

Figures 5 and 6 are the same as figures 1 and 2, but for $M_{\rm BH} = 10^6\,M_\odot$. Figure 6 indicates that the range of the polar angle in which the UFOs are observed (the unshaded region in the plot) is similar to that of $M_{\rm BH} = 10^8\,M_\odot$. Since the density of the wind is roughly two orders of magnitude larger than that for $M_{\rm BH} = 10^8\,M_\odot$ ($\rho \propto M_{\rm BH}^{-1}$), the column density ($\propto \rho r$) in the unshaded region is insensitive to $M_{\rm BH}$. We also find that the velocity and the column density of the matter with $2.5 \leq \log\xi < 5.5$ ($\gtrsim 0.1c$ and $\sim 10^{23}\,\mathrm{cm^{-2}}$) are insensitive to the black hole mass, leading to insensitivity of the UFO probability.

Such a insensitivity is understood as follows. At a given Eddington ratio, the force multiplier, $M(t, \xi)$, required to successfully launch the wind does not depend on the black hole mass. The wind velocity roughly corresponds to the escape velocity at the launching region of $R \sim 30\,R_S$ ($v_r \propto M_{\rm BH}^0$), so that $dv_r/dr$ is proportional to $r^{-1} \propto M_{\rm BH}^{-1}$, leading to $t \propto \rho|dv_r/dr|^{-1} \propto \rho M_{\rm BH}$. On the other hand, we have $\xi \propto L_{\rm X}/\rho r^2 \propto \rho^{-1} M_{\rm BH}^{-1}$ because of $L_{\rm X} \propto L_{\rm Edd} \propto M_{\rm BH}$. Hence, the force multiplier does not depend on the black hole mass when $\rho \propto M_{\rm BH}^{-1}$, and the wind structure and UFO probability are insensitive to the black hole mass.

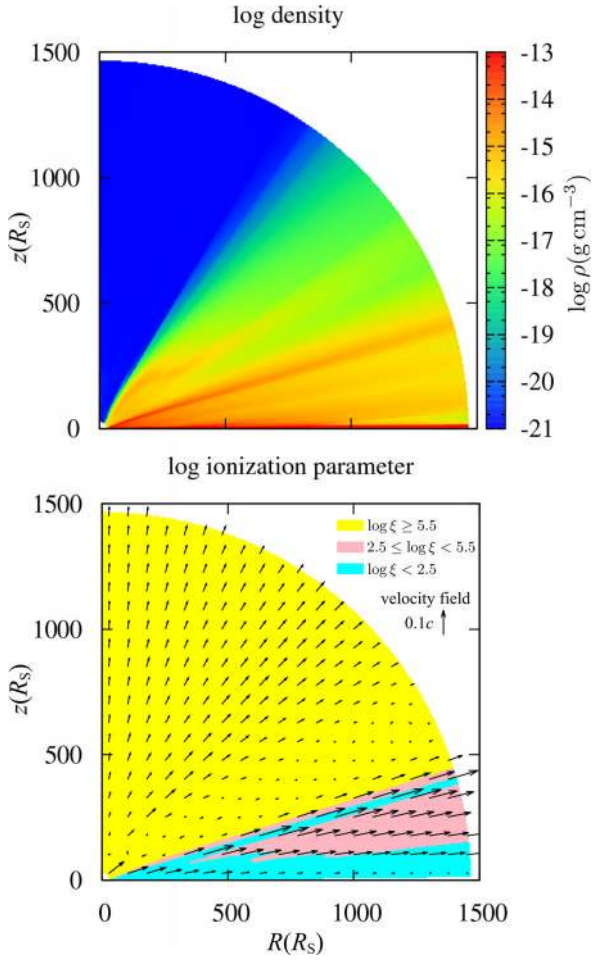


**Fig. 5.** As figure 1, but for $M_{\rm BH} = 10^6\,M_\odot$. (Color online)

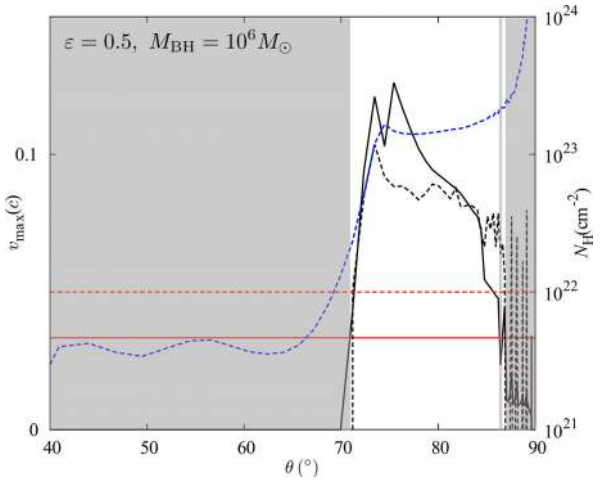


**Fig. 6.** As the top panel of figure 2, but for $M_{\rm BH} = 10^6\,M_\odot$. (Color online)

## 3.4 X-ray luminosity dependence

In order to understand the effect of the X-ray irradiation, we calculate the disk wind for high X-ray luminosity, $f_{\rm X} = 1$ (i.e., $L_{\rm X} = 0.5L_{\rm Edd}$). The disk luminosity and the black hole mass are set to be $L_{\rm D} = 0.5L_{\rm Edd}$ and $M_{\rm BH} = 10^6\,M_\odot$. In this case, since the X-ray luminosity is comparable to the disk luminosity, we should include realistic X-ray radiation force. However, in order to investigate the effect of ionization by the X-ray irradiation, we neglect the X-ray radiation force in the case of $f_{\rm X} = 0.1$. We find that the resultant UFO probability is 34% for $f_{\rm X} = 1$, which is comparable with or slightly larger than that for $f_{\rm X} = 0.1$, 28%.

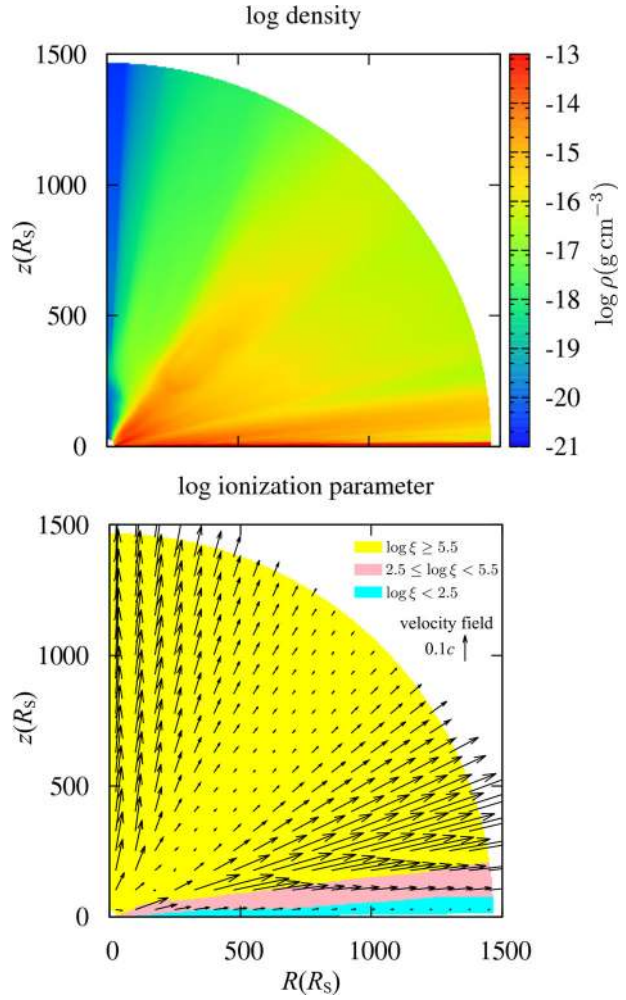


**Fig. 7.** As figure 5, but for $f_{\rm X} = 1$. (Color online)

Figure 7 is the same as figure 5, but for $f_{\rm X} = 1$. We find that the moderate and low ionization regions exist only near the disk surface. This is because the effect of photoionization via X-ray is enhanced. However, the moderately ionized matter near the launching region, $R \sim 30\,R_{\rm S}$, obscures the X-ray source with an angular range of $\theta \gtrsim 70^\circ$. Thus, the UFO probability does not decrease even when we employ $f_{\rm X} = 1$. This is clearly shown in figure 8, which is the same as figure 6, but for $f_{\rm X} = 1$. In the angular range of $\theta \gtrsim 70^\circ$, the column density with $2.5 \le \log\xi < 5.5$ exceeds $10^{22}\,{\rm cm}^{-2}$ so that condition (B) is satisfied. Since condition (A) is also satisfied in this range, the UFO features are observed for an

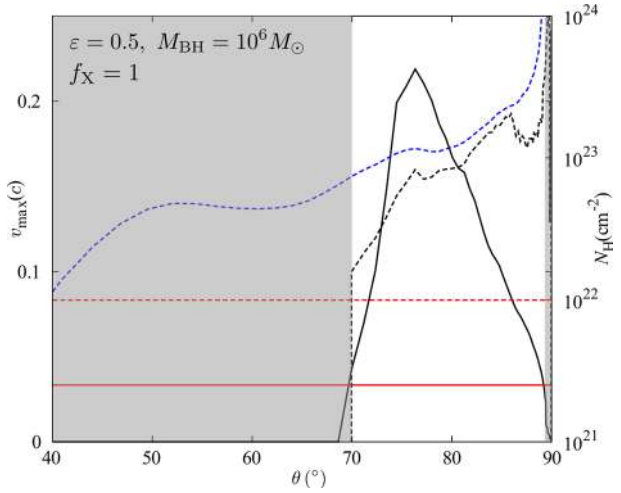


**Fig. 8.** As figure 6, but for $f_{\rm X} = 1$. (Color online)

observer with $\theta \gtrsim 70^\circ$. Such a result is almost the same as the result for $f_{\rm X} = 0.1$.

Here, we note that the high-density region appears in the direction of $\theta \sim 45^\circ$–$70^\circ$, as shown in the top panel of figure 7. However, this region does not raise the UFO probability, since both the ionization state and the velocity disagree with observations (see the bottom panels of figures 7 and 8). In the case of $f_X = 1$, the line force works effectively only in the region where the X-ray is heavily obscured. In this region, the radial component of the disk flux is also diluted so that some of the matter is blown away relatively upward ($\theta \sim 45^\circ$–$70^\circ$) via the line force.

## 4 Discussion

### 4.1 UFO probability, kinetic luminosity, and outflow rate in observations

Our present simulations of line-driven disk winds are roughly consistent with observations of UFOs. Our model shows that the UFO probability is 13%–28% in a wide parameter range of the Eddington ratio and the black hole mass ($\varepsilon \geq 0.1$ and $M_{\rm BH} = 10^{6-9} M_\odot$). We also found that this probability is insensitive to the ratio of the X-ray luminosity to the disk luminosity and the density of the disk surface (see appendix 2). The resulting probability of 13%–28% is roughly comparable to the estimation by Tombesi et al. (2011). They reported the UFO probability to be ~40% based on the frequency of detecting UFOs in the Seyfert galaxies, although the number of UFO samples is still small and the parameter dependence of UFOs is still unknown. As shown in subsection 3.4, the wind is successfully launched when the black hole mass is relatively small ($M_{\rm BH} = 10^6\,M_\odot$) and the X-ray luminosity is large ($L_{\rm X} = 0.5\,L_{\rm Edd}$). This implies that UFO features could appear in the narrow line Seyfert 1 galaxies (NLS1s). In fact, UFO is detected in the NLS1 PG 1211+143 (Pounds et al. 2003; Tombesi et al. 2011).

According to the unified model of AGNs, the torus is thought to be located far outside the accretion disk and obscures the nucleus. If the torus is Compton thin or clumpy, UFO features can be observed even if the torus interrupts the line of sight of the observer. However, if the rotational axis of the accretion disk is aligned with that of the torus, and if the torus is optically thick enough to dilute the UFO features, the range of viewing angles in which the UFOs are observed decreases, reducing the UFO probability. If the outflow coexists with such types of AGNs, we cannot detect the absorption lines from a near equatorial direction. Thus, the UFO probability that we estimated is an upper limit. On the other hand, if the rotational axis of the Compton-thick torus is misaligned with that of the accretion disk, some AGNs, which do not show the UFO features intrinsically, are not detected via the obscuration. This leads to an increase of the UFO probability.

The mass outflow rate and the kinetic luminosity of the line-driven disk winds in the present simulations are also consistent with observations of UFOs. We evaluate the mass outflow rate as $\dot{M}_{\rm out} = 4\pi r^2 \int_0^{89^\circ} \rho v_r \sin\theta d\theta$ at the outer boundary of the calculation box, $r = r_{\rm o}(=1500\,R_{\rm S})$.[1] We find $\dot{M}_{\rm out} = 0.03$–$0.05\,\dot{M}_{\rm acc}$ for a wide range of $\varepsilon$ and $M_{\rm BH}$, where $\dot{M}_{\rm acc}$ is the accretion rate derived from $\dot{M}_{\rm acc} = \varepsilon L_{\rm Edd}/\eta c^2$ with $\eta = 0.06$. This is consistent with that estimated in X-ray observations, i.e. $\dot{M}_{\rm out} \gtrsim 0.05$–$0.1\,\dot{M}_{\rm acc}$ (Tombesi et al. 2012a), although the opening angle of the outflows is observationally less certain.

The kinetic luminosity of the outflows is evaluated by $L_{\rm kin} = 2\pi r^2 \int_0^{89^\circ} \rho v_r^3 \sin\theta d\theta$ at $r = r_{\rm o}$, which is 0.5%–1% of the disk luminosity for $\varepsilon \geq 0.1$ and $M_{\rm BH} \geq 10^7\,M_\odot$. For the cases of $(\varepsilon, M_{\rm BH}) = (0.1, 10^8\,M_\odot)$ and $(0.5, 10^6\,M_\odot)$, the kinetic luminosities are 0.1% and 0.3% of the disk luminosity. Tombesi et al. (2012a) have reported that the kinetic luminosity is about $\gtrsim$0.3% of the bolometric luminosity ($L_{\rm bol}$) by using the bolometric correction $L_{\rm bol} \sim 30\,L_{2\text{–}10}$, with $L_{2\text{–}10}$ being the 2–10 keV luminosity. Since the bolometric luminosity is almost the same as the disk luminosity, ($L_{\rm bol} \sim L_{\rm D}$), our present result agrees with the X-ray observations of UFOs.

In addition, in the model presented by Hopkins and Elvis (2010), the energy outflow rate is required to be larger than 0.5% of the bolometric luminosity to have significant feedback on the surrounding environment. Thus, our present

[1] We exclude the mass flux of 89°–90° from the integration in order to eliminate the influence of the boundary condition of the disk surface. In the region of $r \sim r_{\rm o}$ and $\theta \gtrsim 89^\circ$, the density of the outflow is large as a consequence of the boundary condition that the density is fixed to be $\rho_0$ at the $\theta = 90^\circ$ plane.

simulations imply that the line-driven disk wind could contribute to the feedback on the host galaxies.

Our present study predicts a fraction of quasars show the UFO features, since the disk wind is launched from the disks around supermassive black holes, $M_{\rm BH} \sim 10^9\,M_\odot$, as long as the Eddington ratio is larger than 0.1. However, the disk winds do not appear for less luminous sources with $\varepsilon = 0.01$. This indicates that UFOs are not detected in less luminous AGNs. As we have already mentioned above, NLS1s are the candidate for exhibiting UFO features. This will be verified statistically for larger samples of UFOs in future observations.

### 4.2 Spectral energy distributions

The line force depends on the spectral energy distributions (SEDs). The force multiplier presented by SK90, which is used for the present simulations, is produced by assuming that the 10 keV bremsstrahlung SED determines the ionization states of the various metals and the radiation from a star with an effective temperature of 25000 K contributes to the line force. However, the typical SED of AGNs is the multicolor blackbody superposed with a power law.

In order to assess the difference between the force multiplier of SK90 and that for the AGN SED, we calculate the radiation transfer of the incident AGN SED and estimate the effective force multiplier from the attenuation of the radiative flux. In this calculation, we use a spectral synthesis code, Cloudy (version 13.03, described by Ferland et al. 2013), and adopt the density and velocity gradient ($\rho = 2.04 \times 10^{-16}\,{\rm g\,cm^{-3}}$, $\Delta v_r/\Delta r = 0.0121c/R_{\rm S}$) of a grid cell ($\Delta r = 0.616\,R_{\rm S}$) at around the wind base of the mainstream ($r = 31.8\,R_{\rm S}$, $\theta = 89.^\circ3$), where the line force strongly accelerates the matter and drives the wind. The metal abundance is assumed to be the solar abundance. The incident SED consists of the multicolor disk blackbody and the power law. Here, the multicolor disk blackbody is the superposition of the blackbody radiation from the standard-type disk, of which the effective temperature is described as $1.8 \times 10^5 (r/3\,R_{\rm S})^{-3/4}$ K [see also equation (13)]. We do not take into account the radiation from the region $T_{\rm eff} < 3 \times 10^3$ K ($r > 2315\,R_{\rm S}$) because the effective temperature is too cold to emit the photons largely contributing to the line force. The SED of the multicolor disk blackbody has a peak at around 30 eV. The photon index of the power-law spectrum in the energy range of 0.1–$10^5$ keV is 2.1. The flux of the power law is set to be 10% of the multicolor disk blackbody radiation. We adjust the intensity of the incident radiation as the ionization parameter becomes nearly equal to that of the hydrodynamic simulations ($\xi = 0.773$) in order to focus on the difference in the SED shape. We recognize the ratio of attenuation via metal absorption to that due to electron scattering as the force multiplier for the AGN SED.

As a result, we find that the force multiplier for the AGN SED is about 3.6 times larger than that of SK90. This is because the radiation in a band between 13.6 eV and 1 keV, which is stronger in the AGN SED than in the SED employed in SK90, largely contributes to the line force. Since the radiation in this band is effectively absorbed, such an enhanced line force would not be realized except at the very vicinity of the radiation source. That is, a factor 3.6 is probably an upper limit. Indeed, the optical thickness from the disk surface to the selected grid cell is larger than 10.

To research the effects of the enhancement of the force multiplier, we ran a test model in which the force multiplier is 3.6 times larger than that of SK90 for all the grid cells. As a result, we find that the maximum outflow velocity is around $0.3c$, which is three times larger than the original result ($\sim 0.1c$). The UFO probability is 41%, which is about twice as large as the original UFO probability (20%). This is because the enhanced line force accelerates the wind more upward and the solid angle of the wind increases. The velocity of $\sim 0.3c$ is not inconsistent with observations, and the probability of $\sim$40% fits the estimation by Tombesi et al. (2011). Hence, our disk wind model is consistent with the observed UFO features even if the force multiplier is revised for the AGN SED.

Here we note that, even if the force multiplier for the AGN SED can be proposed, the obtained line force is not rigorous. The spectral shape changes due to the gas–radiation interaction as the radiation passes through the medium. However, this effect is not taken into account in the force multiplier, which is produced based on a fixed spectral shape. The spectrum for each place is obtained by solving the three-dimensional, multi-frequency radiation transfer calculations. Higginbottom et al. (2014) performed the radiation transfer calculations by employing the density structure of the snapshot obtained by PK04. Although they reported the distribution of the ionization parameter in the case of the AGN SED, their post-process calculation could not reveal the wind dynamics. Hydrodynamic simulations coupled with the three-dimensional, multi-frequency radiation transfer calculations are for further study.

Tombesi et al. (2011) reported that the observed absorption lines of Fe XXV and/or Fe XXVI are reproduced by outflowing matter with $2.5 \lesssim \log\xi \lesssim 5.5$, by employing a power-law X-ray spectrum with a photon index, $\Gamma$, of 2, and by considering that the photons in a band from 13.6 eV to 13.6 keV contribute to the ionization of the metals. Since our simulations employ the force multiplier proposed by SK90, the ionization parameter in the present work is evaluated by assuming the 10 keV bremsstrahlung by implication.

To investigate the difference in the absorption lines due to the difference in the employed SED, we use Cloudy and calculate equivalent widths of Fe XXV and Fe XXVI for the 10 keV bremsstrahlung and the power law with $\Gamma = 2$. We focus on a grid cell of $\log\xi \sim 4.0$ located at $r = 95.9\,R_S$ and $\theta = 78.^{\circ}0$. The density is $\rho = 3.8 \times 10^{-17}\,\mathrm{g\,cm^{-3}}$, the grid size is $\Delta r = 7.6\,R_S$, and the outflow velocity is $v_r = 0.028c$. This grid cell includes an angle for which the conditions for detecting UFO (see subsection 3.1) are satisfied. We adjust the intensity of the incident radiation as the ionization parameter is consistent with the result of the hydrodynamic simulations. Thereby, we can focus on the difference in the spectral shape.

As a result, the absorption lines of Fe XXV and Fe XXVI appear for both SEDs, and the equivalent width is not significantly different. We find that the equivalent widths of Fe XXV and Fe XXVI for the 10 keV bremsstrahlung are ∼0.35 times and ∼0.65 times those for the power law. The ratio of the equivalent widths of Fe XXV and Fe XXVI is ∼0.52 times that for the power law.

These results imply that we should take into account the difference in the SEDs of the incident radiation when we try to compare absorption features between the models and observations in great detail. However, this is not serious for the present study, which is roughly researching the $M_{BH}$ dependence and $\varepsilon$ dependence of the UFO probability. The theoretical spectral synthesis adopting a realistic SED is necessary to discuss the absorption features (Schurch et al. 2009; Sim et al. 2010). We will report the simulated absorption features and comparison with the observations of UFOs in a forthcoming paper.

### 4.3 Future works

In our simulations, we simply assume that the radiation from the accretion disk contributes to the line force and the ionization parameter is determined by the radiation from the vicinity of the black hole (approximated as a point source). To study the influence of the ionization photons from the disk, we calculate the ionization parameter by considering the radiation of >13.6 eV from the accretion disk as follows, $\xi_D = 4\pi F_X/n + (4\pi/n)\{(F_{r,\mathrm{ion,thin}}e^{-\tau_X})^2 + F^2_{\theta,\mathrm{ion,thin}}\}^{0.5}$, where the first term indicates the contribution from the central point source and the second term is the contribution from the disk radiation. In the second term, $F_{r,\mathrm{ion,thin}}$ and $F_{\theta,\mathrm{ion,thin}}$ are the $r$-component and the $\theta$-component of the flux above 13.6 eV (or 0.1 keV) emitted from the disk in optically thin media. In the same way as the estimation of the disk flux, the $r$-component of the flux is diluted in accordance with the optical depth measured from the center of the coordinate, $\tau_X$ [see equation (16)].

As a result, for our fiducial model, the highly ionized region ($\log\xi \geq 5.5$) largely expands and moderate and low ionization regions ($2.5 \leq \log\xi < 5.5$ and $\log\xi < 2.5$) appear only near the disk surface. Thus, the UFO probability is reduced to ∼8%, which is about half of our estimation as described in subsection 3.1. Since the low ionization region ($\log\xi < 2.5$), in which the acceleration due to the line force is effective, becomes small from $r \gtrsim 30\,R_S$ and $\theta \gtrsim 78^{\circ}$ (see figure 1) to $r \gtrsim 140\,R_S$ and $\theta \gtrsim 88^{\circ}$, the wind power might decrease.

However, this ionization parameter would be overestimated, because the attenuation of the $\theta$-component of the radiation flux is neglected. The photons with energy ≳13.6 eV are largely diluted in the high-density region around the disk surface in reality, so that the high-ionization region does not expand so much. Indeed, the resulting distribution of the ionization parameter is almost the same as figure 1, if we estimate the ionization parameter by excluding the radiation of 13.6 eV–0.1 keV. If this is the case, both the wind dynamics as well as the UFO probability would not change so much.

We assume axial symmetry in the present simulations, but three-dimensional simulations would be important future work. Recently, time variation of the absorption lines were discovered (e.g., Misawa et al. 2007; Capellupo et al. 2013; Tombesi et al. 2012b). This suggests that the structure of the disk wind changes in time and/or the wind has a non-axial symmetric structure. In one-dimensional as well as two-dimensional calculations, density fluctuations are reported (Owocki & Puls 1999; PSK00). In order to reveal the cause of the time variability, we should perform time-dependent three-dimensional simulations.

Although our simulations investigate the disk wind without solving the structure of the accretion disk, it is important to calculate the wind and the disk self-consistently. We assume that the geometrically thin and optically thick standard disk lies just below our computational domain. The $\theta = 90^{\circ}$ plane is supposed to correspond to the disk surface, and the density on the grids of $\theta = 90^{\circ}$ does not change with time. This implies that the mass and mass accretion rate of the disk do not decrease even if the disk wind is launched. In addition, we treat the accretion disk as an external radiation source, and the photons are steadily emitted from the equatorial plane of the disk. However, in reality, the disk emission would change when the disk wind appears and the mass accretion decreases. The disk and wind should be self-consistently treated by multi-dimensional simulations. Global two-dimensional radiation hydrodynamic/magnetohydrodynamic simulations of the standard disk and the wind were performed by Ohsuga (2006), Ohsuga et al. (2009), and Ohsuga and Mineshige (2011).

## 5 Conclusions

We performed two-dimensional radiation hydrodynamic simulations of line-driven disk winds in AGNs and compared our results to the observational features of UFOs. As a consequence, we revealed that the line force successfully launches the disk wind, and the line-driven disk wind explains major properties of UFOs.

For the fiducial model ($\varepsilon = 0.5$ and $M_{\rm BH} = 10^8\,M_\odot$), the funnel-shaped wind, of which the velocity is $\sim 0.1c$ and the opening angle is $\sim 78^\circ$, is mostly launched from the disk surface of $R \sim 30\,R_{\rm S}$. The column density, the ionization state, and the velocity of the wind nicely agree with observations of UFOs (blueshifted absorption features of Fe XXC and/or Fe XXVI), by which the matter of $>10^{22}\,{\rm cm}^{-2}$ is in the moderate ionization state, $2.5 \leq \log\xi < 5.5$, and is ejected with a velocity of $>10000\,{\rm km\,s}^{-1}$. This result indicates that UFO features are detected when we observe the nucleus from viewing angles $\theta$ between $75^\circ$ and $86^\circ$.

The UFO features could be detected only for an observer with a large viewing angle, at least for an Eddington ratio of $\varepsilon = 0.1$–$0.7$ and black hole mass of $M_{\rm BH} = 10^6$–$10^9 M_\odot$. The angular range of the viewing angle is roughly independent of $\varepsilon$ and $M_{\rm BH}$ or slightly increases with an increase of $\varepsilon$ and a decrease of $M_{\rm BH}$. Our simulations suggest that UFOs are detected with a probability of 13%–28% if we observe luminous AGNs ($\varepsilon \gtrsim 0.1$) like Seyfert galaxies and quasars. The probability is roughly consistent with that inferred from X-ray observations of UFOs, $\sim$40% (Tombesi et al. 2011). The mass outflow rate as well as the kinetic luminosity of the wind also agree with observations (Tombesi et al. 2012a).

The above results do not change significantly if we employ large X-ray luminosity, suggesting that NLS1s are candidates for exhibiting UFO features. In contrast, less luminous AGNs do not show UFOs, since the wind is not launched for $\varepsilon \lesssim 0.01$.

## Acknowledgements

We would like to thank Masayuki Umemura for useful discussions. Numerical computations were carried out on the Cray XC30 at the Center for Computational Astrophysics, CfCA, at the National Astronomical Observatory of Japan. M. N. is supported by a Research Fellowship from the Japan Society for the Promotion of Science (JSPS) for Young Scientists (25·10444). This work is supported in part by Grants-in-Aid of the Ministry of Education, Culture, Sports, Science, and Technology (MEXT) (24740127, K. O.; 23540267, K. W.). Part of this research has been funded by MEST Strategic Programs for Innovative Research (SPIRE) Field 5 "The origin of matter and the universe," Joint Institute for Computational Fundamental Science (JICFuS), and the Center for the Promotion of Integrated Sciences (CPIS) of Sokendai.

## Appendix 1. Dynamics of disk wind

In the extended view of the top panel in figure 1, We find streams of dense matter (slimline winds) along the direction of $\theta \sim 78^\circ$ (orange). This slimline wind, which possesses almost all the momentum of the outflow, is the mainstream of the disk wind. The matter of the mainstream is lifted relatively upward around the wind base (launching region of the wind) and turns in the radial direction, producing the funnel-shaped wind. The reason why the slimline wind is kept narrow is probably that the matter of the mainstream moves with supersonic velocity. Here, we discuss the acceleration mechanism of the matter around the wind base and the bending mechanism of the mainstream.

The force multiplier, $M(\xi, t)$, as a function of the ionization parameter, $\xi$, and the local optical depth parameter, $t$, is shown in figure 9. The solid red line with red filled circles shows the location in $t$–$\xi$ space obtained by tracing the $R = 30\,R_{\rm S}$ line from $z \sim 0$ to $z \sim 0.2$ ($\theta \sim 89.^\circ 98$) based on our results. The red circles roughly move from upper left to lower right with increasing altitude, since the density decreases with $z$, and since $t$ and $\xi$ are almost proportional to $\rho$ and $\rho^{-1}$ [see equations (11) and (19)]. Note that a surge of $t$ at the upper-left region is caused by $|dv_r/dr|$ being very close to null at the disk surface. The red line passes through the region $M \gtrsim 0.1$ when $\xi \sim 10$–$100$ and $t \sim 10^{-3}$–$10^{-2}$, where the enhanced line force assists the matter to move upward.

Near the disk surface ($z \lesssim 0.01\,R_{\rm S}$), the local optical depth parameter is too large for the force multiplier to exceed 0.1. In this region, the matter is not accelerated by the line force. The density distribution is adjusted so as to keep the balance between the gravitational force and sum of the gas pressure force and the radiation force via electron scattering. Although the matter moves upward because of $M \gtrsim 0.1$ at around $z \sim 0.01$–$0.07\,R_{\rm S}$, the overionization reduces the force multiplier to less than 0.1 at a higher region ($z \gtrsim 0.07\,R_{\rm S}$). Thus, a "traffic jam" is induced because the upward velocity at $z \sim 0.1$–$0.2\,R_{\rm S}$ decreases. The density increases because of this traffic jam so that the ionization parameter becomes smaller, making the force multiplier larger again (see $z \sim 0.2\,R_{\rm S}$, where $\log\xi \sim 2.3$, $\log t \sim -3$, and $M \sim 0.6$). The enhanced line force blows the high-density matter outward, which is the origin of the mainstream of the wind. At $z \gtrsim 0.2\,R_{\rm S}$, the matter gradually falls down.

Next, we focus on the bending of the mainstream. In figure 10, the directions of the velocity (solid line with filled circles), the total force (dashed line with open circles), and the radiation force (dash-dotted line with filled squares) along the mainstream are shown as a function of $R$. Here, the total force means the sum of the radiation force, the

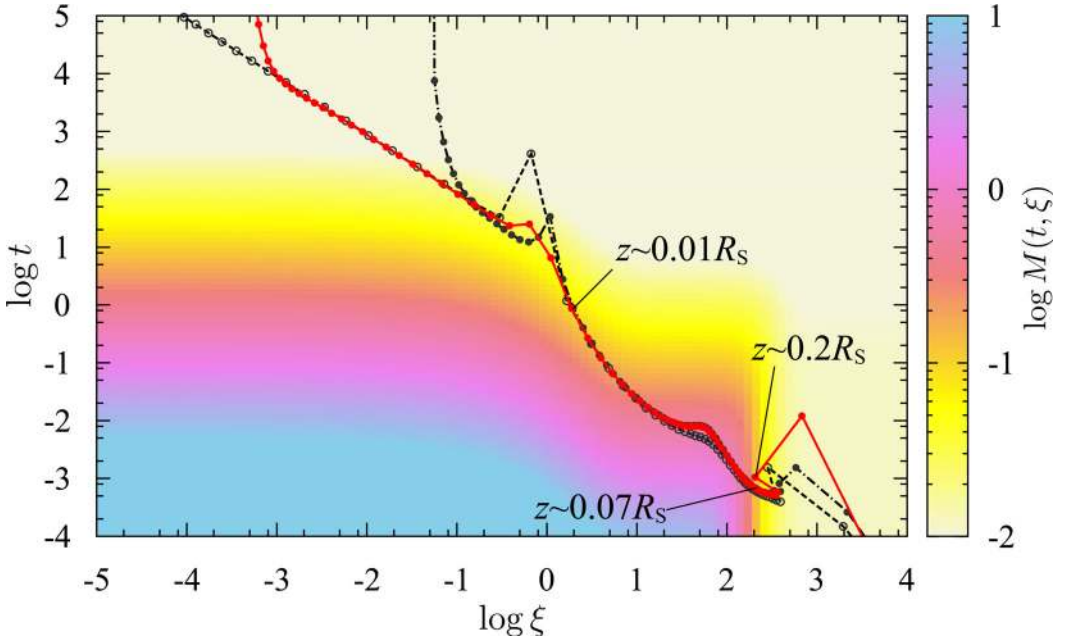


**Fig. 9.** Force multiplier in the space of the ionization parameter and the local optical depth parameter. The solid red line with red filled circles shows the location in $t$–$\xi$ space obtained by tracing the $R = 30\,R_{\rm S}$ line from $z \sim 0$ to $z \sim 0.2$ ($\theta \sim 89.^{\circ}98$) based on our results for the fiducial model ($\varepsilon = 0.5$, $M_{\rm BH} = 10^8\,M_{\odot}$, $f_{\rm X} = 0.1$, and $\rho_0 = 10^{-9}\,{\rm g\,cm^{-3}}$). The black dashed line with the open circles and the black dash-dotted line with the filled circles are the same as the red line, but for $\rho_0 = 10^{-7}\,{\rm g\,cm^{-3}}$ and $\rho_0 = 10^{-11}\,{\rm g\,cm^{-3}}$. (Color online)

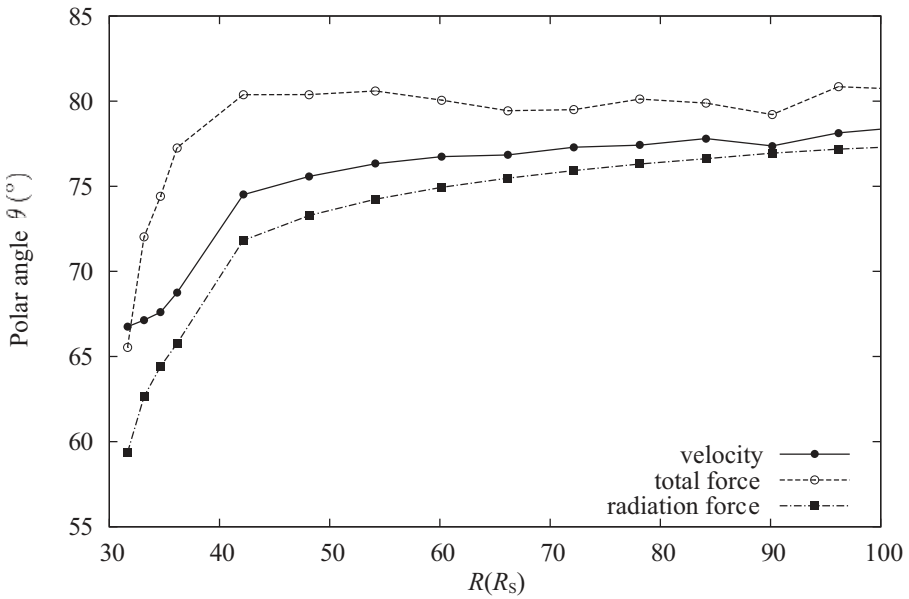


**Fig. 10.** Polar angles of the directions of the velocity (solid line with filled circles), the total force (dashed line with open circles), and the radiation force (dash-dotted line with filled squares) along the dense streaky structure (see figure 1). The total force includes the radiation force, the gravitational force, and the centrifugal force (other than the gas pressure force). The horizontal axis is the distance from the central black hole along the disk surface.

gravitational force, and the centrifugal force. The gas pressure force is negligible. It is found that the direction of the velocity gradually shifts from $\theta \sim 65^{\circ}$ to $\sim 78^{\circ}$. This means that the matter is lifted relatively upward near the wind base and the outflow turns in the radial direction with an increase of $R$. Thus, the mainstream of the wind becomes funnel-shaped.

Such a bending of the stream is caused by the radiation force in cooperation with the centrifugal force. Since the radiation comes from the disk surface, the $\theta$-component of

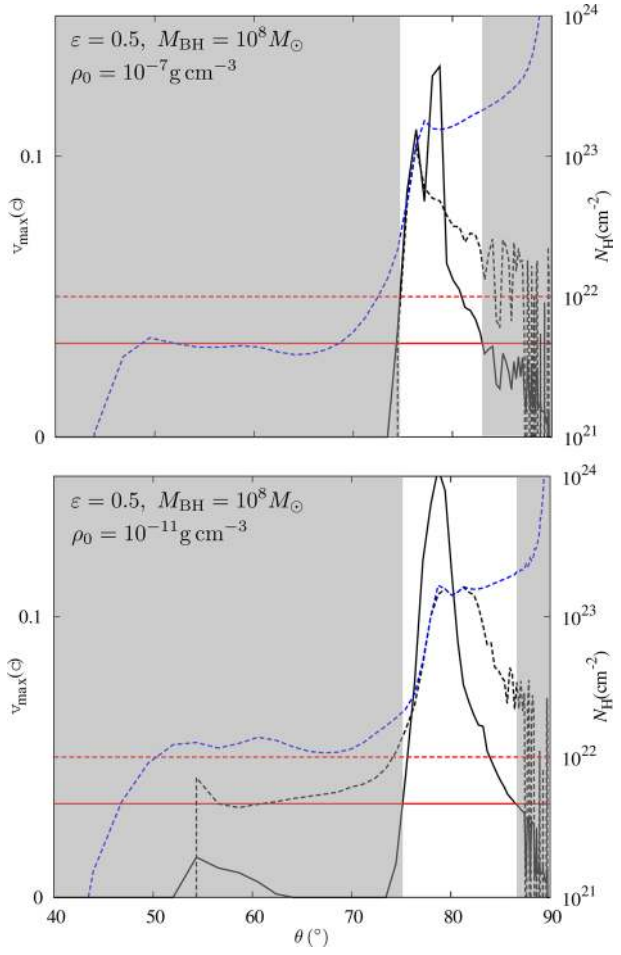


**Fig. 11.** As the top panel of figure 2, but for $\rho_0 = 10^{-7}\,{\rm g\,cm^{-3}}$ (top panel) and $\rho_0 = 10^{-11}\,{\rm g\,cm^{-3}}$ (bottom panel). (Color online)

the radiation force is non-trivial at the inner region but, in contrast, gets close to null at the outer region. Thus, the direction of the radiation force including the line force changes from $\theta \sim 60^\circ$ to $\sim 78^\circ$ (almost the $r$-direction). The direction of the total force is different from that of the radiation force at $R \lesssim 50\,R_{\rm S}$, but both get closer at $R \gtrsim 50\,R_{\rm S}$. This is because the centrifugal force is considerable only near the launching region. Hence, the wind launched in the direction of $\theta \sim 65^\circ$ at the wind base gradually changes direction and finally just flows along the direction of the radiation force (total force), $\sim 78^\circ$.

## Appendix 2. Dependence on density at disk surface

The wind structure does not change so much if we change $\rho_0$. Figure 11 is the same as figure 2 but for $\rho_0 = 10^{-7}\,{\rm g\,cm^{-3}}$ (top panel) and for $\rho_0 = 10^{-11}\,{\rm g\,cm^{-3}}$ (bottom panel). In both cases, the funnel-shaped disk wind with opening angle of $\theta \sim 78^\circ$ appears, and the UFO probability is 20% for $\rho_0 = 10^{-11}\,{\rm g\,cm^{-3}}$ and 14% for $\rho_0 = 10^{-7}\,{\rm g\,cm^{-3}}$. Although the unshaded region is slightly narrow for $\rho_0 = 10^{-7}\,{\rm g\,cm^{-3}}$, we find that the column density and the velocity with $2.5 \le \log\xi < 5.5$ are insensitive to $\rho_0$ in the unshaded region (see figures 2 and 11).

In figure 9, the black dashed line with the open circles and the black dash-dotted line with the filled circles show the locations in $t$–$\xi$ space obtained by our calculations for $\rho_0 = 10^{-7}\,{\rm g\,cm^{-3}}$ and for $\rho_0 = 10^{-11}\,{\rm g\,cm^{-3}}$. We find that the force multiplier differs depending on $\rho_0$ in the vicinity of the disk surface. However, as the density decreases with the altitude, the three lines get close and converge at $z \gtrsim 0.01\,R_{\rm S}$. This simply explains why the wind structure as well as the UFO probability does not change so much if we change $\rho_0$ in the present simulations.

## References


Allen, J. T., Hewett, P. C., Maddox, N., Richards, G. T., & Belokurov, V. 2011, MNRAS, 410, 860
Blandford, R. D., & Payne, D. G. 1982, MNRAS, 199, 883
Capellupo, D. M., Hamann, F., Shields, J. C., Halpern, J. P., & Barlow, T. A. 2013, MNRAS, 429, 1872
Castor, J. I., Abbott, D. C., & Klein, I. 1975, ApJ, 195, 157
Elvis, M. 2000, ApJ, 545, 63
Everett, J. E., & Murray, N. 2007, ApJ, 656, 93
Ferland, et al.2013, Rev Mex. Astron. Astrophys., 49, 137
Foltz, C. B., Weymann, R. J., Morris, S. L., & Turnshek, D. A. 1987, ApJ, 317, 450
Gayley, K. G. 1995, ApJ, 454, 41
Gibson, R. R., et al. 2009, ApJ, 692, 758
Hamann, F., Korista, K. T., & Morris, S. L. 1993, ApJ, 415, 541
Harten, A., Lax, P. D., & van Leer, B. 1983, SIAMR, 25, 35
Higginbottom, N., Proga, D., Knigge, C., Long, K. S., Matthews, J. H., & Sim, S. A. 2014, ApJ, 789, 19
Hopkins, P. F., & Elvis, M. 2010, MNRAS, 401, 7
Kato, S., Fukue, J., & Mineshige, S. 2008, Black-Hole Accretion Disks—Towards a New Paradigm, (Kyoto: Kyoto University Press)
Konigl, A., & Kartje, J. F. 1994, ApJ, 434, 446
Misawa, T., Eracleous, M., Charlton, J. C., & Kashikawa, N. 2007, ApJ, 660, 152
Nomura, M., Ohsuga, K., Wada, K., Susa, H., & Misawa, T. 2013, PASJ, 65, 40
Ohsuga, K. 2006, ApJ, 640, 923
Ohsuga, K., & Mineshige, S. 2011, ApJ, 736, 2
Ohsuga, K., Mineshige, S., Mori, M., & Kato, Y. 2009, PASJ, 61, L7
Owocki, S. P., & Puls, J. 1999, ApJ, 510, 355
Pounds, K. A., Reeves, J. N., King, A. R., Page, K. L., O'Brien, P. T., & Turner, M. J. L. 2003, MNRAS, 345, 705
Proga, D., & Kallman, T. R. 2004, ApJ, 616, 688 (PK04)
Proga, D., Stone, J. M., & Drew, J. E. 1998, MNRAS, 295, 595
Proga, D., Stone, J. M., & Drew, J. E. 1999, MNRAS, 310, 476
Proga, D., Stone, J. M., & Kallman, T. R. 2000, ApJ, 543, 686 (PSK00)

Risaliti, G., & Elvis, M. 2010, A&A, 516, 89
Schurch, N. J., Done, C., & Proga, D. 2009, ApJ, 694, 1
Shakura, N. I., & Sunyaev, R. A. 1973, A&A, 24, 337
Sim, S. A., Proga, D., Miller, L., Long, K. S., & Turner, T. J. 2010, MNRAS, 408, 1396
StevensI., R., & Kallman, T. R. 1990, ApJ, 436, 599 (SK90)
Takahashi, H. R., & Ohsuga, K. 2013, ApJ, 772, 127
Tombesi, F., Cappi, M., Reeves, J. N., & Braito, V. 2012a, MNRAS, 422, L1
Tombesi, F., Cappi, M., Reeves, J. N., Palumbo, G. G. C., Braito, V., & Dadina, M. 2011, ApJ, 742, 44
Tombesi, F., Cappi, M., Reeves, J. N., Palumbo, G. G. C., Yaqoob, T., Braito, V., & Dadina, M. 2010, A&A, 521, A57
Tombesi, F., Sambruna, R. M., Marscher, A. P., Jorstad, S. G., Reynolds, C. S., & Markowitz, A. 2012b, MNRAS, 424, 754
Weymann, R. J., Morris, S. L., Foltz, C. B., & Hewett, P. C. 1991, ApJ, 373, 23
Zubovas, K., & King, A. 2013, ApJ, 769, 51

Special feature: Latest Advances in Computational Astrophysics (No. 9)